Modeling active fault systems and seismic events by using a Fiber Bundle model. Example case: Northridge aftershock sequence.

Marisol Monterrubio-Velasco[1], Ramón Zúñiga[2], Carlos Carrasco-Jiménez[1], Víctor Márquez-Ramírez[2], and Josep de la Puente[1]

[1]Barcelona Supercomputing Center. Jordi Girona 29, C.P. 08034, Barcelona (Spain)
[2]Centro de Geociencias, Universidad Nacional Autónoma de México, Juriquilla, Querétaro, 76230, México

Correspondence: M. Monterrubio-Velasco (marisol.monterrubio@bsc.es)

Abstract. Earthquake aftershocks display spatio-temporal correlations arising from their self-organized critical behavior. Dynamic deterministic modeling of aftershock series is difficult to carry out due to both the physical complexity and uncertainties related to the different parameters which govern the system. Nevertheless, numerical simulations with the help of stochastical models such as the Fiber Bundle (FBM) permit the use of an analog of the physical model that produces a statistical behavior with many similarities with real series. FBM are simple discrete element models that can be characterized by using few parameters. In this work, a new model based on FBM that includes geometrical faults systems is proposed. Our analysis focuses on aftershock statistics in space, time and magnitude domains. To analyze the model behavior a parametric study is carried out. Moreover, we analyzed the synthetic aftershock sequences properties assuming initial load configurations and suitable conditions to propagate the rupture. As an example case, we have modeled a set of real active faults related to the Northridge, California, earthquake sequence. We compare the simulation results to statistical characteristics from the Northridge sequence determining which range of parameters in our FBM version reproduce the main features observed in real aftershock series. In order to reproduce statistical characteristics of the real sequence larger π_{frac} values ($0.85 < \pi_{\mathrm{frac}} < 0.95$) and very low values of P ($0.0 < P \le 0.08$) are needed. This implies the important corollary that a very small departure from an initial random load configuration (computed by P), and also a large difference between the load transfer from on-fault segments than by off-faults (computed by π_{frac}), is required to initiate a rupture sequence which conforms to observed statistical properties such as the Gutenberg-Richter law, Omori law and fractal dimension.

1 Introduction

Most earthquakes occur when adjacent blocks move along fractures in the Earth's crust, as a consequence of stress build-up arising from the regional strain and the stress change caused by a preceding earthquake or by the tectonic stress accumulation (Stein et al., 1994). These fractures, or faults, are discontinuous geological features consisting of a number of discrete segments (Segall and Pollard, 1980), which can be up to hundreds of kilometers in total length. Faults are the weakest parts of the crust and thus are more likely to release accumulated stresses, by means of slipping, than non-fractured crust. Earthquakes may occur many times on the same fault over millions of years. Known active faults have ruptured several times in the last 120,000

years and are considered likely to move again (Wallace, 1981). It has been observed that earthquakes are strongly correlated in space around the active fault systems (Kroll, 2012). In addition, fault systems have a statistical self-similar structure over a wide range of scales (Kagan and Knopoff, 1980; Sadovskiy et al., 1984; Hirata and Imoto, 1991) which can be described by means of fractal geometry, as introduced by Mandelbrot and Pignoni (1983). Earthquakes follow power statistical laws

5   for their observed scaling properties such as the Gutenberg-Richter (GR) distribution (Gutenberg and Richter, 1942; Scholz, 2002), the Modified Omori (MO) law , (Omori, 1894; Godano et al., 1996; Hirata and Imoto, 1991) or the fractal dimension of their spatial distribution (Turcotte, 1997; Roy and Ram, 2006)

Geometrical fractal structures such as faults, arise from self-organized criticality (SOC) phenomena over large temporal periods (Bak and Creutz, 1994). SOC systems have been studied as a means to explain seismicity (Barriere and Turcotte, 1994;

10 Scholz, 1991). In particular, cellular-automata type models have been used to describe SOC behaviour in Earthquake series (Aki, 1965; Barriere and Turcotte, 1994). The Fiber Bundle Model, FBM, is one such cellular-automata model which provides conceptual and numerical description of the rupture process in heterogeneous and complex materials, such as the Earth's crust (Peirce, 1926; Daniels, 1945; Coleman, 1956; Hansen et al., 2015).

In this article, our objective is to study the effect of including geometrical fault systems in a FBM algorithm, over the

15 statistical parameters of simulated seismic aftershock catalogs. We test the FBM's ability to capture the statistics coming from empirical laws (the GR law, the fractal capacity dimension, the MO law, and the Hurst exponent) by means of a parametric study. As an example case we considered the Northridge aftershock sequence (January 17,1994,Mw=6.7). The geometry of the fault system related to this sequence is incorporated in the model. The statistical characteristics from the Northridge aftershock sequence are compared with the statistics obtained in synthetic catalogs. Finally, we study the event productivity as function of

20 the on-fault (or weakling areas) and off-fault parameters.

2   Background

This section provides a general description of the Fiber Bundle model and the statistical relations used in this work.

2.1   Fiber Bundle Model, FBM: general description

The basic components necessary to construct an FBM model include: (Andersen et al., 1997; Phoenix and Beyerlein, 2000;

25 Pradhan and Chakrabarti, 2003; Sornette, 1989; Kloster et al., 1997):

1. Discretization: The study area is represented as a discrete set of cells ("fibers") organized on an n-dimensional and regular lattice (square, triangular, etc.).

2. Failure Law: The rupture of the individual elements or fibers is described by a probability distribution function.

3. Loading Sharing Rule: Once a cell fails, its load is shared by the neighboring fibers. The range and type of the interaction

30   of fibers is an important component of the model since it has a substantial effect on the behavior of the overall rupture (Kun et al., 2006b, a; Pradhan et al., 2010). For example, the most common sharing rules are:

– Equal Load Sharing (ELS), for which the load is equally redistributed over all intact cells (Krajcinovic, 1996; Turcotte et al., 2003).

– Local Load Sharing (LLS), in this scheme the load is equally redistributed over its nearest neighbours in the lattice. This rule favors stress concentrations along failed regions and promotes that neighbors reach a critical rupture state .

There are two versions of the FBM model that simulate material rupture by different effects: static and dynamic. In the static version, the fiber strength is time independent (Vázquez-Prada et al., 1999; Kun et al., 2006a; Pradhan et al., 2010) and the interaction between the load sharing rule and the initial heterogeneity in the stress threshold generates avalanches of ruptures (Pradhan et al., 2010), being this feature a used resource in our simulation. On the other hand, the dynamic FBM version studies the material rupture considering time-dependent processes, such as stress-rupture, creep-rupture, static-fatigue or delayed-rupture (Coleman, 1956; Moral et al., 2001b). In this work we will use a dynamic FBM with LLS in the probabilistic formulation developed in Moreno et al, (2001).

2.1.1 Probabilistic FBM

The FBM starts by discretizing a hypothetical surface in a bidimensional array ($N_x \times N_y$).

Experimental studies support the Weibull distribution function as a relation that describes the stress behavior of materials subjected to a constant load, assigning a hazard rate as follows (Coleman, 1956; Phoenix, 1978; Phoenix and Tierney, 1983; Vázquez-Prada et al., 1999; Moreno et al., 2001):

$$\kappa(\sigma) = \nu_0 \left(\frac{\sigma}{\sigma_0} \right)^\rho,$$
(1)

where ν_0 is the hazard rate under stress σ_0, and the ρ exponent is the Weibull index, a non-dimensional constant with values in the range $2 \leq \rho \leq 50$ (Yewande et al., 2003; Kun et al., 2006a; Nanjo and Turcotte, 2005). In the present work we use a dimensionless representation of quantities, so that we can use normalized stresses and equation 1 can be written as $\kappa(\sigma) = \sigma^\rho$, following (Moreno et al., 2001; Monterrubio-Velasco et al., 2017). Gómez et al. (1998) introduced a probabilistic approach as an alternative formulation to the dynamic FBM which we follow here.

In the initial state, the load of the cells in the bundle is assigned following a uniform distribution $\sigma_{(x,y)} = U[0,1), x = 1, ..., N_x$, and $y = 1, ..., N_y$. This assumption simulates an initial heterogeneity in the load cells properties. The hazard rate assigned at each cell is computed using Eq. 1. (Moreno et al., 1999; Pradhan et al., 2010). Furthermore, a rupture probability, $F_{(x,y)}$, is computed for each cell and at each step. This value is load dependent and is defined by,

$$F_{(x,y)} = \sigma^\rho_{(x,y)} \delta,$$
(2)

where δ is the time interval (or inter-event time), until the next rupture occurs valid for any load share rule (Moral et al., 2001a), computed as

$$\delta = \frac{1}{\displaystyle\sum_{x=1,y=1}^{N_x,N_y} \sigma_{(x,y)}^{\rho}} \, .\tag{3}$$

δ is a dimensionless quantity since $\sigma_{(x,y)}$ and ρ are dimensionless. In particular, we use Eqs. 2, 3 and 6, to compute the

5   rupture probability and the inter-event time and in our algorithm.

2.2   Statistical and Fractal relations

In order to quantify the resemblance between synthetic catalogs and real seismic catalogs, we use statistical measures that are relevant for evaluating the SOC behavior. These measures are represented by power laws in magnitude (Gutenberg-Richter, GR, law), in time (Modified Omori, MO, law) or in space (*e.g.* fractal dimension). In Appendix A1 we introduce these relations,

10   describing their applicability, as well as the interpretation, and the methods of quantification. We summarize the characteristics, the acronym, and usefulness of the empirical relations used in this work in Table 1.

3   Fault systems model

In previous work Monterrubio-Velasco et al. (2017), developed a FBM version, to simulate spatial and magnitude aftershocks patterns. However, the model did not incorporate the information of the fault geometry which is a fundamental property to

15   describe a particular tectonic region. In this work, we add the fault system geometry and prescribe a parameter that quantifies the "weakness" of such faults, *i.e.* the capacity to produce load concentrations that generates rupture. This parameter is the load transfer, π, which controls the amount of load distributed from a failed cell to its neighbors. Since the seismic rupture is not conservative, the parameter $\pi(x,y)$ defines the percentage of load lost at each step. The output of the model is a synthetic catalog with statistical properties that depend on the input parameters.

20   ## 3.1   Algorithm

Following the general assumptions proposed in Correig et al. (1997) and modified by Monterrubio-Velasco et al. (2017), the main algorithm requires a definition of the 2D Cartesian grid of a rectangular domain Ω of $N_x \times N_y = N_T$ square cells. The domain is a planar representation of the study area. We then require to define a discrete value of load $\sigma_{(x,y)}$, the load-transfer value $\pi_{(x,y)}$ and the rupture probability $F_{(x,y)}$ (Eq. 2) at each cell in $x \in [1,...,N_x]$ and $y \in [1,...,N_y]$. A local load sharing

25   rule including the eight nearest neighbors is consider.

As mentioned in section 2, the initial load distribution is taken from a uniform distribution function, where values are in the range [0,1). No external load is received after the initial load assignation. Note that this model version describes the relaxation process after a mainshock. Therefore we do not discuss or simulate neither mainshock nor foreshocks. The load increase in

a cell is due to internal load transfer processes. Moreover, the initial load values are ordered according to a probability value P. P=0 represents a random spatial distribution of initial loads (heterogeneous), and P=1 implies the most homogeneous distribution in agreement with a proxy of Coulomb stress changes produced by a main event in the center of Ω (Monterrubio-Velasco et al., 2017). Also, a threshold load, $\sigma_{th} \equiv 1$, is defined. When the load in a cell exceeds this threshold load, a critical

5   point is reached (called *avalanches*). Consequently, that cell has to fail and distribute its respective percentage of load ($\sigma_T = \sigma_F * \pi$) to its eight neighbors. Perpendicular neighbors will receive the largest amount of load (($\sigma_T * 0.98)/4$) while diagonal neighbors get a load of ($\sigma_T * 0.02)/4$. If more than one cell exceeds σ_{th}, the cell to fail is that which exhibits the maximum load. The parameters ρ (Weibull index) (Eq. 1) and P (heterogeneity of the initial load distribution) have global extent and need to be prescribed initially in order to run a scenario. Both $\sigma_{(x,y)}$ and $F_{(x,y)}$ are dynamic variables, since will be modified

10   during the algorithm execution.

An FBM simulation should be terminated when any cell in the system is unable of exceed σ_{th}. We have empirically determined that the total number of steps k_{max} when this situation occurs is typically $k_{max} \approx 3N_T/4$. Beyond this value the system no longer generates load that overpass σ_{th}. Hence we take this value as a terminal condition in our simulations.

Throughout the iterations of the simulation we identify two possible outcomes: *normal events*, *i.e.* minor or background

15   ruptures, and *avalanches*, *i.e.* a collections of spatio-temporally clustered events that result in large rupture. We remark that, in the present work, *avalanches* are actual secondary ruptures, whereas *normal* are minor events of negligible magnitude. The consecutive rupture of *avalanches* events will produce a rupture cluster with a size determined by their area in [cells] units $S(N_A)$. After the simulation is finished, we obtain a synthetic seismic catalog which includes: the number of simulated earthquakes, N_A, as well as their area $S(N_A)$ (number of events that behaves a single rupture) and occurrence time t_A (Eq.

20   3), together with their spatial location (x, y). We will later discuss how the avalanche size $S(N_A)$ can be converted into magnitude. It should be noted that two realizations with identical parameters result in different seismic catalogs due to the random component in the initial load.

The procedure is detailed explained in the pseudo-codes provided in Appendix A2.

The $\pi_{(x,y)}$ value is statically distributed according to the given fault system geometry. The values of $\pi_{(x,y)}$ are chosen to

25   have either a background value (π_{back}) or a fault value (π_{frac}), *i.e.* only one of two values are possible for each cell.

3.2   Methodology

The discrete planar faults of a particular region are modeled by using an image of the real faults system. This image is mapped in the domain Ω (see example in Fig. 2). A parametric study is employed to determine the best range of values to produce synthetic catalogs with appropriate statistical characteristics. In this work, we use the following parameters: $\rho = 30$, $\sigma_{th} = 1$,

30   $\sigma_D = 0.02/4$ and $\sigma_N = 0.98/4$. We also fix a background $\pi_{back} = 0.65$ value for all non-faulted cells and assume a square grid, with same lateral size in *x*-axis and *y*-axis, i.e. $N_x = N_y = \sqrt{N_T}$. These values are considered from the results obtained in Monterrubio-Velasco et al. (2017).

The map of faults has a real physical size in km^2. So, after executing the algorithm 1, in the post-processing analysis, we assign an area at each cell in km^2, namely A_{cell}. To compute the avalanche area $S(N_A)$ in km^2 we use the relation,

$$A_j = S(j) \cdot A_{\text{cell}}, \tag{4}$$

for $j = 1, ..., N_A$. We computed an equivalent magnitude using the scale magnitude-area relation proposed by (Hanks and Bakun, 2008) in Eq. 5.

$$M_{\text{w}} = 4/3 \log A + (3.07 \pm 0.04), \tag{5}$$

where $A_j, for j = 1, ..., N_A$ is the rupture area expressed in km^2 and M_W is the moment magnitude. This relation is specific for events in a Crustal-Plate-Boundary tectonic regime (Stirling M.W., 2012).

Careful attention has been given to minimum magnitudes which depend on size of the cell A_{cell} (i.e. are proportional to N^{-2}). In order to make results comparable for different grid sizes, we filter out events rupturing less than a minimum amount of cells for the finer grids.

We are left with three freely varying parameters for our study. Based on previous results we use N_x = [180,240,300] cells, π_{frac} = [0.6, 0.65, 0.7, 0.75, 0.8, 0.85, 0.9, 0.95, 1.0] and P = [0.0,0.08,0.16,0.24,0.32,0.38] (Monterrubio-Velasco et al., 2018). This results in 162 samples in the parametric space.

The epicentral location of the simulated aftershocks is the position of the first *avalanche event* $((E_x(j), E_y(j)))$ in the cluster. The time of occurrence $T(j)$ is,

$$T(k) = \sum_{i=1}^{k} \delta_i, \tag{6}$$

where $k = 1, ..., k_{\text{max}}$. We define $\Delta(r)$ as series of the euclidean distance between two consecutive epicenters, and $\tau(t)$ the inter-event time series corresponding to two consecutive avalanches (see Eq. 6).

Table 2 summarizes the model parameters, and list their search range and a brief definition.

4   Test case: Northridge aftershock sequence

In order to validate and compare our synthetic results with real seismicity, we modeled as an example case the fault system geometry and seismicity related to the Northridge aftershock sequence. The Northridge mainshock ($M_W = 6.7$) occurred on January 17, 1994 at 4:31 UTC. The earthquake shook the San Fernando Valley, which is 31 km northwest of Los Angeles, near the community of Northridge. This earthquake is the largest recorded in the Los Angeles metropolitan area in the last century. The depth of the hypocenter was 18 ± 1 km. The seismic moment, M_{w}, was estimated at $1.58 \cdot 10^{23}$ N·m, with a stress drop of 27 MPa (Thio and Kanamori, 1996).

The mainshock occurred due to the rupture of a previously unrecognized blind reverse fault with a moderate southward dip (Savage and Svarc, 2010; U.S.G.S., 1994). The Northridge mainshock occurred at a fault belonging partly to a large fault system in the Transverse ranges. This fault system is under compression in the NNW direction related to the "big bend" of the San Andreas fault (Norris and Webb, 1990; Hauksson et al., 1995). The Northridge earthquake was followed by a sequence

5 of aftershocks, between the 17th of January and the 30th of September 1999, including 8 aftershocks of magnitude $M_w \geq 5$ and 48 of $4 \leq M_w \leq 5$. We computed the statistical parameters of the aftershocks using the data recorded by the Southern California Seismic Network. We consider the aftershock time period from the mainshock (January 17, 1994 at 4:31 UTC) until one year afterwards (January 17, 1995). In space, we consider events that occur in a square area of 0.6 ° x 0.6° taking as center the mainshock epicenter 1 (Turcotte, 1997). We also assumed that the faulting area is the same independently of the model

10 domain size Ω. However, the number of cells modify the size of each cell, resulting in 0.077 km^2, 0.043 km^2, and 0.027 km^2, for N_x = [180,240,300] cells respectively.

In Table 3 we show the statistical parameters for the Northridge sequence computed for different threshold magnitudes from $M_{min} = 1.5$ to $M_{min} = 3.5$. These values will be used as a reference to determine the sets of FBM parameters that best reproduce the Northridge statistics. Fig. 3 show the fitting of GR law, MO law, and Hurst exponents (H_Δ ,H_τ and H_{Mag}),

15 for different minimum magnitude M_{min} >1.5, >2.0, >2.5, >3.0, >3.5. We note that Wiemer and Wyss (2000) calculated the minimum magnitude of completeness in the Los Angeles area as $M_c \approx 1.5$.

5   Results

We divide the results and their analysis in three domains:

- Space: fractal capacity dimension, D_0, for the epicentral distribution of synthetic earthquakes, and Hurst exponent for
20 epicentral distance between consecutive synthetic earthquakes, $H(\Delta)$.

- Magnitude: b-value, maximum avalanche size $\max S(N_A)$, mean Magnitude and maximum Magnitude.

- Time: Inter-event times $H(\tau)$ and MO parameters (p, c, K).

5.1   Parametric analysis over the synthetic series

5.1.1   Fractal dimensions of synthetic catalogs

25 The first analysis is related to the fractal capacity dimension, D_0. We observe (Fig. 4) that as N increases D_0 becomes more sensitive to P because the larger the epicentral area, the more abundant and scattered are the events, and the effect of P over the simulated events increases. The effect of an increase in P is a reduction of D_0. On the other hand, as P tends to zero, the events are more scattered because randomness in the initial load causes sparsity in the event distribution. Moreover, π_{frac} does not seem to have a large impact in D_0 across our experimental range. We also find that for $P \leq 0.16$ and $\pi_{frac} > 0.9$ (for all N

30 values) our FBM simulations yield a D_0 compatible with that computed for the Northridge series with a $M_{min} \approx 2$ (Table 3).

5.1.2   *b*-value, *mean* and *maximum* magnitude of synthetic catalogs

The b-value is clearly influenced by all three parameters (N, P and π_{frac}). For example, small N tends to produce similar b-values independently of P. On the other hand, as N increases, the b-value is more sensitive to P. The different b-values as a function of N might be due to two possible causes: 1) the number of events included in the statistical fit and 2) the size of the avalanches, $S(N_A)$. In Fig. 6 (a) we observe that as P increases the maximum magnitude also increases, also modifying the frequency-magnitude distribution and the b-value. As an example, Fig. 7 shows the frequency-magnitude for $P = [0, 0.08, 0.16, 0.24, 0.32, 0.38]$, $\pi_{\mathrm{frac}} = 0.9$, $\pi_{\mathrm{frac}} = 0.65$, and $N = 300$. We observe that as P increases the productivity of intermediate size events decreases, and the maximum magnitude increases. Large P values imply that the probability to find cells with large loads clustered in the middle increases (Monterrubio-Velasco et al., 2017). So in this condition it is more likely to generate larger earthquakes. This behavior is similar to that observed in the characteristic earthquake distribution (Wesnousky, 1994). In the case of finer grids, if we consider an initial random load distribution $P = 0$, we can observe that b approaches when $\pi_{\mathrm{frac}} > 0.90$. This last observation is important to justify the influence of fractures in the b-value since it is closer to the theoretical value when the contrast in "non-conservative" properties is significant. From Fig. 5, we observe that the best range of b-values, similar to that obtained for Northridge sequence is for $P < 0.16, \pi_{\mathrm{frac}} > 0.90$, and $N \geq 240$.

From Fig. 6 (b) we observe that the mean magnitude is independent of π_{frac} and to a lesser extent of P. It is worth pointing out that the b-values are similar to those shown in Table 3 when $M_{\mathrm{min}} \approx 2$ or 2.5. Fig. 6 (b) shows that, in our model, an aftershock with a magnitude such as that of the Northridge largest aftershock magnitude ($M_W = 5.9$) is obtained for a non-unique combination of parameters. When $P > 0.08$ and $\pi_{\mathrm{frac}} > 0.7$ this magnitude is overestimated.

5.1.3   Hurst exponent of synthetic catalogs

Figs. 8 (a) and (b) show the results of the Hurst exponent for inter-event distance $H(\Delta)$ and inter-event time $H(\tau)$ (Eq. A6). The re-scaled range analysis of the $\Delta(r)$ series reveals their independence on N and π_{frac} but shows a slightly higher dependence with P. In general as P increases $H(\Delta)$ also increases. As P decreases $H(\Delta) \to 0.5$ implying that the system tends to a random behavior of the inter-event epicentral distribution. However $H(\Delta)$ always remains similar to the values of Table 3 for $P \approx 0$. Gkarlaouni et al. (2017) showed that the seismicity in the Corinth rift (Greece) corresponded to $H(\Delta) \to 0.5$ as the threshold magnitude decreased.

The analysis of $H(\tau)$ reveals in general values > 0.5 which implies a persistence in the dynamic system of inter-event times, *i.e.* the behavior of future inter-event time can be extrapolated from previous behavior. As P increases the persistence of $H(\tau)$ also increases, which may be related with the MO trend (discussed below). The influence of π_{frac} over $H(\tau)$ is not clear, however the number of events decreases when we take a larger cutoff magnitude and this fact could affect the re-scaled range statistics.

5.1.4 MO parameters in synthetic catalogs

The MO empirical law requires careful analysis in our FBM implementation. First of all, we must take into account that we are using dimensionless time (see eq. 3). Our cumulative time, T_j is computed using Eq. 6. For example, considering the input values of $P = 0.08$, $\pi_{\mathrm{frac}} = 0.90$, $N_x = 180$, if we include all simulated events (minor events and aftershocks) together, (e.g.

5   Figure 9 *(a)*, we get a satisfactory MO fit with $p =1.1$, $c =1.5$, $K = 11991.3$, and $rms = 675.0$. But if we use only the time occurrence of the simulated aftershocks ($S(N_A)$), the parameters depart from the expected trend (e.g., Fig. 9 *b*), obtaining $p = 1.9$, $c =4.9$, $K = 1571.9$, and $rms =10.8$. Two regions are distinguished in Fig. 9 *(b)* where we can see that the density of events in the blue region is much larger than in the green. Therefore the MO fit is deviated adjusting for events in the blue region. It is known that real aftershocks do not always follow a single MO decay trend (Utsu and Ogata, 1995). Moreno et al. (2001)

10   developed an alternative model to understand this phenomenon called *Leading* and *Cascades* (LA-CAS) events. This model proposes a separation of earthquakes in two groups: One that strictly follows the MO hypothesis (called *Leading* aftershocks, LA) and those called *Cascades* which are the events that occur between two consecutive LAs. Note that to obey the MO relation, the inter-event times must increase monotonically. LA events satisfies this assumption. Monterrubio et al. (2015) tested the $LA - CAS$ algorithm to study the temporal behavior of three real aftershock sequences. The MO fit of Figure 9

15   resembles the behavior found in Monterrubio et al. (2015). After segregating the events in LA and CAS, we obtain a better fit to the MO relation for the LA series (Fig. 10, LA: $p = 0.9$, $c = 0.1$, $K = 5.1$, $rms = 1.2$). The full results of the MO relations are shown in Figs. 11 (a) and (b).

The MO parametric results provide information of the temporal behavior in the simulated series. We observe that $P < 0.08$ implies p and c values close to the expected Norhtridge values (see Table 3). However, the number of events after segregating

20   LA and CAS decreases, so the value of K is much lower than expected. These results indicate that series with an initial load configuration organized with a probability $P > 0.08$ depart from a typical MO behavior. This occurs because the aftershock series produced with larger initial organization probabilities ($P > 0.08$) tend to generate temporal series with very short elapsed times (Eq. 3), and larger avalanche clusters, which does not follow a typical MO distribution. The closest behavior to the observed MO parameters of Northridge (Table 3) occur for $P \leq 0.08$ and $\pi_{\mathrm{frac}} > 0.7$.

25   ## 5.2 Trigger and shadow regions

The load-transfer value $\pi(x, y)$ is highly relevant to reproduce temporal, magnitude, and spatial patterns of real series (Monterrubio et al., 2015). Considering this fact, we are also interested in studying the implication of this value in the aftershock productivity, in particular for off-fault regions. To test the productivity as a function of π_{bkg}, two extreme values are considered for $\pi_{\mathrm{bkg}} = 0.25$ and $\pi_{\mathrm{frac}} = 0.65$. In Fig. 12 we observed that activity in background (non faulting) cells largely decreases for

30   small π_{bkg} values. This occurs because for low π values the probability to produce an event with larger ruptured area decreases (Fig. 13). The results suggests that variations in π_{bkg} for different regions of the domain can lead to producing shadow and triggered regions, giving a scenario closer to a real case (King et al., 1994; **?**; Hainzl et al., 2014). However, in this study,

our first attempt is more focused on the parametric implications of the fault regions included in the model. We expect that the integration of triggered and shadow regions will be plausible in future implementations to improve the results.

5.3 Results Summary: Synthetic catalogs

Lastly, we estimated the error between the real and synthetic statistical values using a measure similar to the euclidean distance r_{E-Mmin}. However, in our case r_{E-Mmin} is referred to a normalized parametric space because the different units in the parameters, and it is defined as:

$$r_{E-Mmin} = \sqrt{\sum_{i=1}^{9} \left[\frac{(ps[i] - ps_{Mmin}[i])}{ps[i]} \right]^2}, \tag{7}$$

where,

$$ps = [D_0, <M_w>, b-value, M_{\max}, M_{\min}, H(\Delta), H(\tau), p, c]$$

is the vector that contains the values of the series generated with a given set of input parameters P, π_{frac}, and N. Similarly, the vector ps_M contains the values for the Northridge series considering four different minimum magnitudes $M_{\min} = [1.5, 2.0, 2.5, 3.0]$ (Table 3). We computed $r_{E-M_{\min}}$ for the 162 combinations of P, π_{frac}, and N, each one with 3 realizations. In Table 4 we show the minimum of $r_{E-M_{\min}}$ for $M_{\min} = [1.5, 2.0, 2.5, 3.0]$. The minimum euclidean distance occurs when we consider the NOR series with $M_{\min} = 2.0$. It is worth mentioning that the minimum magnitude of the synthetic aftershocks considered in this work is also ≈ 2.0. The results show that the most appropriate set of parameters to model this data series is $P = 0$, $\pi_{\mathrm{frac}} = 0.90$ using $N = 300$ cells.

Fig. 14 shows the euclidean distance between the sequence generated by NOR using the set of parameters obtained with $M_{\min} = 2.0$ and its real values.

In Fig. 15 we show an example of a spatial distribution of events and its related GR relation (Fig. 16), using the set $P = 0$, $\pi_{\mathrm{frac}} = 0.95$ and $N = 300$. As shown in Fig. 15, the largest aftershocks have its epicenter on fault's cells ($M > 3.5$). The epicenters are depicted with a blue star. This scatter plot also shows that the smallest events usually occur spread out. The relation of the magnitude and the cumulative number of events, generated in this example, shows a GR fit with a similar b-value to that the computed in Table 3.

6 Discussion

The main goal of this study was to integrate prior knowledge of the spatial geometry of faults in the implementation of the FBM algorithm, improving the model previously proposed in Monterrubio-Velasco et al. (2017). The main advantage of the present model is the reduced number of equations to be solved in comparison with deterministic models for similar purposes, and the low number of parameters used to describe the model dynamics ($\pi_{\mathrm{frac}}, \pi_{\mathrm{bkg}}, \rho, P$ and N_T). To validate our model we used as an example the geometry of the Northridge fault system and the statistics of the aftershocks. Note that this model version

describes the relaxation process after a mainshock. Therefore we do not discuss or simulate neither mainshock nor foreshocks. In particular, we explored the power laws' exponents D_0, b, H, p parameters in relation to the model parameters (Section A1).

Other models have been proposed to describe with simplified mechanism the statistics of earthquakes, such as the "Two Fractal Overlap Model" (Bhattacharya et al., 2009) or the "Olami, Feder and Christesen (OFC)" model (Olami et al., 1992). In particular, the OFC model has a very similar algorithmic behavior to our proposed model (Kawamura et al., 2012). But our model yields similar results with fewer input parameters and it is simpler to implement.

As a statistical modelling tool, we need a parametric analysis to properly fit observational data. In our study we have searched the range of values that generate synthetic series capable of reproducing the statistical relations of real aftershock series. In particular, we explored three (π_{frac}, P and N) of the five free parameters, to quantify their leading role in the model. We point out that π_{bkg} and ρ are assumed as constants following results in Monterrubio et al. (2015) and Monterrubio-Velasco et al. (2017). In agreement with Monterrubio-Velasco *et al.*, monterrubio2015aftershock, we also confirm that the transferred load value π is the most critical parameter in order to reproduce temporal, magnitude, and spatial patterns of real series. Our results also suggest that variations in π for different regions of the domain might generate shadow regions (King et al., 1994; Stein, 1999; Hainzl et al., 2014). The initial load configuration, controlled by P, results determinant to describe the final statistical features in the model. In particular, the results indicate that P and π_{frac} are inversely proportional. As we increase π_{frac}, a small value of P is required to reproduce aftershocks statistics. If the fault geometry is not considered in the model ($\pi_{\text{bkg}} = \pi_{\text{frac}}$), the particular range of $0.60 < \pi < 0.70$ found in (Monterrubio-Velasco et al., 2017) is required to captures statistical patterns. However, an optimization of the parametric search using classification machine learning techniques can be very useful in this stochastic model. Considering the example of Northridge our results suggest that the best combination which approach to real cases depends on the minimum magnitude. The usefulness of this stochastic model is its capability to generate a large number of scenarios with statistical properties similar to real cases, with low computational cost and a low number of free parameters.

7 Conclusions

We present a model which fulfills statistical properties of aftershock series incorporating fault system geometry. We choose statistical relations which describe the aftershocks' behavior in space, magnitude and time. By means of a parametric study we have found the range of values that generate synthetic series capable of reproducing the statistical relations of real aftershock events. In particular, we have used the Northridge fault system geometry and aftershock sequence as a study case. We conclude that the initial load configuration (quantified by parameter P), which specifies the randomness in the background load· distribution, and the ratio of transferred load for a faulting cell π_{frac} are the key parameters that control the earthquake's statistical patterns in FBM simulated events. Moreover, these parameters are complementary, i.e. in absence of fault geometry information ($\pi_{\text{frac}} = \pi_{\text{back}}$), values in the range $0.08 < P < 0.32$ ensure statistical compatibility with real aftershocks. In particular, for $\pi_{\text{frac}} = \pi$ and $N = 180$ we recover the results obtained previously without fault information (Monterrubio-Velasco et al., 2017). On the other hand, when fault geometry is available, as in the case of the Northridge fault system, the results obtained in this work show that, in order to reproduce statistical characteristics of the real sequence, larger π_{frac} values ($0.85 < \pi_{\text{frac}} < 0.95$)

and very low values of P ($0.0 < P \leq 0.08$) are needed. This implies the important corollary that a very small departure from an initial random load configuration is required to initiate a rupture sequence which conforms to observed statistical properties such as the Gutenberg-Richter Law, Omori Law and fractal dimension. In summary, the proposed model is a useful tool to model aftershock scenarios by means of its inherent statistical patterns in time, space, and magnitude. Moreover, the model

5   circumvents the high complexity related with the derivation of deterministic models of earthquake rupture phenomena. We also conclude that, although the FBM algorithm is quite simple, the model is powerful enough to provide simulated data statistically consistent with real scenarios. Our model can be an alternative to the study of the complex behavior of earthquakes. Future work will focus on optimization of the parametric search using machine learning techniques and extensions towards a 3D FBM version.

10   **Appendix A: Appendix A**

A1   Statistical and fractal relations

A1.1   Fractal dimension

Fractured systems, including lithospheric faults, are scale invariant in a large scale range being characterized by the power law (Turcotte, 1997; Mandelbrot, 1989). The fractal dimension is an important parameter used to characterize fracture patterns in

15   heterogeneous materials (Hirata and Imoto, 1991). In seismicity, it provides a quantitative measure of the spatial clustering of epicenters and hypocenters (Roy and Ram, 2006). There are many fractal dimension definitions and descriptions used to characterize a dynamical system, for example the capacity dimension, D_c, (Nanjo et al., 1998; Legrand et al., 2004), the information dimension D_I, or the correlation dimension, D_G (Grassberger and Procaccia, 1983). For the purpose of our study, we will use only the capacity dimension, D_c

20   The generalized fractal dimension D_q is used to compute different fractal dimensions (Eneva, 1994).

$$D_q = \lim_{r \to 0} \frac{log C_q(r)}{log(r)}, \tag{A1}$$

where

$$C_q(r) = \left\{ \frac{1}{N} \sum_{i=1}^{N} \left[\frac{1}{N-1} \sum_{j \neq i} \mathcal{H}(r - \|x_i - x_j\|) \right]^{q-1} \right\}^{\frac{1}{q-1}}, \tag{A2}$$

with q is a positive or negative real number, N the number of samples, $\|x_i - x_j\|$ the inter-event distance for consecutive

25   events, $\mathcal{H}$ the Heaviside step function and r a threshold distance value to evaluate $\mathcal{H}$. With this method we compute the probability of a pair of points in the system being closer than the threshold r. Eq. A2 has the property that $D_{(q=0)} = D_c$, $D_{(q=1)} = D_I$ and $D_{(q=2)} = D_G$ (Barriere and Turcotte, 1994) assumed that a fractal spatial distribution of earthquakes implies

a fractal distribution of faults. Turcotte turcotte1997fractals showed that the capacity dimension of epicentral and hypocentral distributions yield a power law (or fractal) with $D_0 \approx 1.6$ and $D_0 \approx 2.5$, respectively.

A1.2 Re-scaled range analysis and Hurst exponent

The rescaled range (R/S) analysis, and more specifically the Hurst exponent H (Hurst, 1965) offers a criterion for evaluating

5   the predictability of a complex dynamic system (Feder, 1988; Goltz, 1997). The R/S analysis can be interpreted as a method to measure the long-range correlation in time series. Some applications of this fractal technique in different fields of geophysics and geology are given in Korvin (1992) and Turcotte (1997). R/S analysis on earthquake sequences was first implemented by Lomnitz (1994), and applied to an analysis of the seismicity of the South Iberian Peninsula (Lana et al., 2005), the Corinth rift and Mygdonia graben in Greece (Gkarlaouni et al., 2017) or aftershocks in Southern California (Monterrubio-Velasco, 2013).

10   Being $X \in (X_1, X_2, ..., X_n)$ a set of observations in a time series, the mean, m, of the series is computed and a mean adjusted series is created, following

$$Y_t = X_t - m \,, \tag{A3}$$

for $t = 1, ..., n$. Then a cumulative deviate series Z can be computed as

$$Z_t = \sum_{i=1}^{t} Y_i \,, \tag{A4}$$

15   Then R/S is the ratio between the range R_t and standard deviation S_t, where the range is computed as

$$R_t = \max(Z_1, Z_2, ..., Z_t) - \min(Z_1, Z_2, ..., Z_t) \,, \tag{A5}$$

and S_t is the standard deviation of $Z_1, ..., Z_t$. Hurst used the following power-law relationship to determine the predictability of time series (Hurst, 1965)

$$\log(R_t/S_t) = C + H \cdot \log(t) \,, \tag{A6}$$

20   where $H = 0.5$ indicates randomness in the series, i.e. the samples are not correlated with one another. $H > 0.5$, indicates some degree of predictability, or temporal persistence in the system. Lastly, $0 < H < 0.5$ indicates antipersistence, i.e. an increasing (decreasing) trend in the past implies a decreasing (increasing) trend in the future (Correig et al., 1997).

A1.3 Gutenberg-Richter law

The Gutenberg-Richter (GR, sometimes referred to as Gutenberg-Richter Ishimoto-Ida) law is considered one of the major manifestations of self-organized criticality in a natural system. It has been observed that, earthquake magnitude distributions fit a GR power law (Gutenberg and Richter, 1942)

$$\log_{10} N(\geq M) = a - bM \,, \tag{A7}$$

where $N(\geq M)$ is the cumulative number of events with magnitude greater or equal than M. The slope b describes the ratio between small and large magnitude events and is usually in the range $0.65 < b < 1.05$ (Evernden, 1970; Ozturk, 2012) whereas a is proportional to the earthquake productivity (i.e. the seismicity rate).

In particular, b is one of the most useful statistical parameters for describing the size scaling properties of seismicity. For
10
example, Ozturk (2012) concludes that this parameter can be used to differentiate tectonic regions. Similarly, Zuniga and Wyss (2001) used the b-value to identify most and least likely locations of earthquakes in the Mexican subduction zone.

In the rest of the present work we apply the maximum likelihood method to estimate b (Aki, 1965)

$$b = \frac{log10(e)}{|\langle M \rangle - (M_{\min} - \Delta M/2)|} \,, \tag{A8}$$

where $M_{\min}$ is the minimum magnitude of events considered in the study, ΔM is related with the precision of the recorded
15
magnitude, in our case we consider $\Delta M = 0.1$. The error of b is computed as (Shi and Bolt, 1982),

$$\sigma(b) = 2.30 b^2 \sigma(\langle M \rangle) \,, \tag{A9}$$

where

$$\sigma(\langle M \rangle) = \sum_{i=1}^{n} (M_i - \langle M \rangle)^2 / n(n-1) \,, \tag{A10}$$

A1.4 Modified Omori law

The temporal behavior of aftershocks is commonly described by the modified Omori (MO) law (Omori, 1894; Utsu and Ogata, 1995) defined as

$$n(t) = \frac{K}{(t + c)^p} \,, \tag{A11}$$

where $n(t)$ is the generation rate of aftershocks at a time t after the mainshock, whereas K, c, and p are parameters to be determined. The p parameter controls the aftershock activity decay and is related to the physical conditions in the fault zone

(Kisslinger, 1996; Ogata, 1999). Its value is typically $p \approx 1$. The constant c eliminates the uniqueness of occurrence rate at $t = 0$ (Kisslinger, 1996), the productivity K is a constant that depends on the total number of aftershocks. Then the cumulative number of aftershocks, $N(t)$, of the earthquake count at time t since the mainshock at $t = 0$, can be obtained by integrating Eq. A11 resulting in

$$5 \quad N(t) = \int_0^t n(s)ds = \begin{cases} K\{ln(t+c) - ln(c)\} & p = 1 \\ \\ \frac{K\left[(c+t)^{(1-p)} - c^{(1-p)}\right]}{1-p} & p \neq 1 \end{cases}, \tag{A12}$$

A2 Algorithm

The main Algorithm (A2.1), for each step k, updates the rupture probability F of each cell, finding the cell boasting the largest load and then finding whether that load exceeds the given load threshold σ_{th}. If so, rupture is initiated and an avalanche occurs due to recurrent load transfer and rupture of neighboring cells. Whenever no cell has sufficient load to reach σ_{th} a regular, i.e. minor, event is triggered, which ensures load transfer and hence makes more likely an avalanche, i.e. major, event in the next time steps. The initialization step is shown in Algorithm 2 (A2.2) and the rupture process is depicted in Algorithm 3 (A2.3). Notice that rupture relies in a transfer-ratio weight σ_N for the horizontal and vertical transfer and σ_D for diagonal transfer, which are further global parameters to prescribe.

A2.1 Main algorithm

Algorithm 1 Main FBM algorithm. The processes **initialize** and **rupture** are described in Algorithms 2 and 3, respectively.

$k = 0;\ n_A = 0;\ T_1 = 0$
initialize
$\delta_1 = \left(\sum_{i,j} \sigma(i,j)^\rho \right)^{-1}$
while $k < k_{\max}$ **do**
  $k = k + 1$
  for $(i,j) \in \Omega$ **do**
    $F(i,j) = \sigma(i,j)^\rho \delta_k$
  end for
  $(l,m) = \{(i,j) \in \Omega \mid \sigma(i,j) = \max(\sigma)\}$
  if $\sigma(l,m) > \sigma_{\mathrm{th}}$ **then**
    $n_A = n_A + 1$
    rupture(l,m)
    if $n_A = 1$ **then**
      $S(n_A) = 0$
    else
      $S(n_A) = S(n_A) + 1$
    end if
    $t(n_A) = T_k;\ S(n_A) = 0;\ E_x(n_A) = l;\ E_y(n_A) = m$
  else
    if $n_A \neq 0$ **then**
      $N_A = n_A$
      $S(N_A) = S(n_A)$
      $T(N_A) = t(1)$
      $n_A = 0;\ S(n_A) = 0$
    end if
    find (p,q) sample of $F(i,j)$
    rupture(p,q)
  end if
end while

A2.2 Algorithm 2

Algorithm 2 FBM initial load, where $\mathcal{U}$ is the uniform density function and $\mathcal{U}_D$ its discrete (integer) counterpart

---

initialize
for all $(i,j) \in \Omega$ **do**
    $\alpha = \mathcal{U}(0,1)$
    if $0 < \alpha \leq P$ **then**
        $\sigma(i,j) = \sigma_I(i,j)$
    else
        $r_i = \mathcal{U}_D(1,N_x)$
        $r_j = \mathcal{U}_D(1,N_y)$
        $\sigma(r_i,r_j) = \sigma_I(i,j)$
    end if
end for

A2.3 Algorithm 3

Algorithm 3 Performs the rupture process of a single FBM cell of indexes (p,q)

---

rupture(p,q)
$\sigma(p,q) = \pi(p,q)\,\sigma(p,q)$
for $(r,s) \in \{(1,0),(0,1),(-1,0),(0,-1)\}$ **do**
    $\sigma(p+r,s+q) = \sigma(p+r,s+q) + [\sigma_N \sigma(p,q)]$
end for
for $(r,s) \in \{(1,1),(1,-1),(-1,1),(-1,-1)\}$ **do**
    $\sigma(p+r,s+q) = \sigma(p+r,s+q) + [\sigma_D \sigma(p,q)]$
end for
$\sigma(p,q) = 0$
$\delta_k = \left(\sum_{i,j} \sigma(i,j) \right)^{-1}$ (Eq. 3)
$T_k = \sum_{l=1}^{k} \delta_l$

Competing interests. no competing interests are present

Acknowledgements. M.M.V thanks CONACYT for funding this research project. This project has received funding from the European

5 Union's Horizon 2020 research and innovation programme under the Marie Skłodowska-Curie grant agreement No 777778 MATHROCKS

and from the Spanish Ministry Project TIN2016-80957-P. Initial funding for the project through grant UNAM-PAPIIT IN108115 is also gratefully acknowledged. The research leading to these results has received funding from the European Union's Horizon 2020 Programme under the ChEESE Project (https://cheese-coe.eu/), grant agreement n° 823844.

References

Aki, K.: Maximum likelihood estimated of b in the formula log N=a-bM abd its confidence limits, Bull Earthq Res Inst Tokyo Univ, 43, 237–239, 1965.

Andersen, J. V., Sornette, D., and Leung, K.-t.: Tricritical behavior in rupture induced by disorder, Physical Review Letters, 78, 2140, 1997.

5 Bak, P. and Creutz, M.: Fractals and self-organized criticality, in: Fractals in science, pp. 27–48, Springer, 1994.

Barriere, B. and Turcotte, D.: Seismicity and self-organized criticality, Physical Review E, 49, 1151, 1994.

Bhattacharya, P., Chakrabarti, B. K., Samanta, D., et al.: Fractal models of earthquake dynamics, arXiv preprint arXiv:0906.1931, 2009.

Coleman, B. D.: Time dependence of mechanical breakdown phenomena, Journal of Applied Physics, 27, 862–866, 1956.

Correig, A. M., Urquizu, M., Vila, J., and Marti, J.: Analysis of the temporal ocurrence of seismicity at deception Island (Antarctica). A

10   nonlinear approach, Pure and Applied Approach, 149, 553–574, 1997.

Daniels, H.: The statistical theory of the strength of bundles of threads. I, in: Proceedings of the Royal Society of London A: Mathematical, Physical and Engineering Sciences, vol. 183, pp. 405–435, The Royal Society, 1945.

Eneva, M.: Monofractal or multifractal: a case study of spatial distribution of mining-induced seismic activity, Nonlinear Processes in Geophysics, 1, 182–190, 1994.

15 Evernden, J.: Study of regional seismicity and associated problems, Bulletin of the Seismological Society of America, 60, 393–446, 1970.

Feder, J.: Fractals (physics of solids and liquids), Plennum, New york, 1988.

Gkarlaouni, C., Lasocki, S., Papadimitriou, E., and George, T.: Hurst analysis of seismicity in Corinth rift and Mygdonia graben (Greece), Chaos, Solitons & Fractals, 96, 30–42, 2017.

Godano, C., Alonzo, M., and Bottari, A.: Multifractal analysis of the spatial distribution of earthquakes in southern Italy, Geophysical Journal

20   International, 125, 901–911, 1996.

Goltz, C.: Fractal and chaotic properties of earthquakes, in: Fractal and Chaotic Properties of Earthquakes, pp. 3–164, Springer, 1997.

Gómez, J., Moreno, Y., and Pacheco, A.: Probabilistic approach to time-dependent load-transfer models of fracture, Physical Review E, 58, 1528, 1998.

Grassberger, P. and Procaccia, I.: Measuring the strangeness of strange attractors, Physica D: Nonlinear Phenomena, 9, 189–208, 1983.

25 Gutenberg, B. and Richter, C. F.: Earthquake magnitude, intensity, energy, and acceleration, Bulletin of the Seismological Society of America, 32, 163–191, 1942.

Hainzl, S., Moradpour, J., and Davidsen, J.: Static stress triggering explains the empirical aftershock distance decay, Geophysical Research Letters, 41, 8818–8824, 2014.

Hanks, T. and Bakun, W.H., .: M-log A observations of recent large earthquakes, Bulletin of the Seismological Society of America, 98,

30   490–494, 2008.

Hansen, A., Hemmer, P. C., and Pradhan, S.: The fiber bundle model: modeling failure in materials, John Wiley & Sons, 2015.

Hauksson, E., Jones, L. M., and Hutton, K.: The 1994 Northridge earthquake sequence in California: Seismological and tectonic aspects, Journal of Geophysical Research: Solid Earth, 100, 12 335–12 355, 1995.

Hirata, T. and Imoto, M.: Multifractal analysis of spatial distribution of microearthquakes in the Kanto region, Geophysical Journal Interna-

35   tional, 107, 155–162, 1991.

Hurst, H. E.: Long term storage, An experimental study, 1965.

Kagan, Y. and Knopoff, L.: Spatial distribution of earthquakes: the two-point correlation function, Geophysical Journal International, 62, 303–320, 1980.

Kawamura, H., Hatano, T., Kato, N., Biswas, S., and Chakrabarti, B. K.: Statistical physics of fracture, friction, and earthquakes, Reviews of Modern Physics, 84, 839, 2012.

5   King, G. C., Stein, R. S., and Lin, J.: Static stress changes and the triggering of earthquakes, Bulletin of the Seismological Society of America, 84, 935–953, 1994.

Kisslinger, C.: Aftershocks and fault zone properties, Geophys J Int, 38, 1–36, 1996.

Kloster, M., Hansen, A., and Hemmer, P. C.: Burst avalanches in solvable models of fibrous materials, Physical Review E, 56, 2615, 1997.

Korvin, G.: Fractal models in the earth sciences, Elsevier Science Ltd, 1992.

10 Krajcinovic, D.: Damage mechanics, vol. 41, Elsevier, 1996.

Kroll, K. A.: Complex Faulting in the Yuha Desert: Implications for Fault Interaction, University of California, Riverside, 2012.

Kun, F., Hidalgo, R. C., Raischel, F., and Herrmann, H. J.: Extension of fibre bundle models for creep rupture and interface failure, International journal of fracture, 140, 255–265, 2006a.

Kun, F., Raischel, F., Hidalgo, R., and Herrmann, H.: Extensions of fibre bundle models, Modelling critical and catastrophic phenomena in
15   geoscience, pp. 57–92, 2006b.

Lana, X., Martinez, M., Posadas, A., and Canas, J.: Fractal behaviour of the seismicity in the Southern Iberian Peninsula, Nonlinear Processes in Geophysics, 12, 353–361, 2005.

Legrand, D., Villagómez, D., Yepes, H., and Calahorrano, A.: Multifractal dimension and b value analysis of the 1998–1999 Quito swarm related to Guagua Pichincha volcano activity, Ecuador, Journal of Geophysical Research: Solid Earth, 109, 2004.

20 Lomnitz, C.: Fundamentals of earthquake prediction, Wiley, 1994.

Mandelbrot, B. B.: Multifractal measures, especially for the geophysicist, Pure and applied geophysics, 131, 5–42, 1989.

Mandelbrot, B. B. and Pignoni, R.: The fractal geometry of nature, vol. 173, WH freeman New York, 1983.

Monterrubio, M., Lana, X., and Martínez, M. D.: Aftershock sequences of three seismic crises at southern California, USA, simulated by a cellular automata model based on self-organized criticality, Geosciences Journal, 19, 81–95, 2015.

25 Monterrubio-Velasco, M.: Análisis estadístico y comportamiento fractal de las réplicas sísmicas del Sur de California, 2013.

Monterrubio-Velasco, M., Zúñiga, F., Márquez-Ramírez, V., and Figueroa-Soto, A.: Simulation of spatial and temporal properties of aftershocks by means of the fiber bundle model, Journal of Seismology, https://doi.org/10.1007/s10950-017-9687-8, 2017.

Monterrubio-Velasco, M., Carrasco-Jiménez, J., Castillo-Reyes, O., Cucchieti, F., and de la Puente J.: A Machine Learning Approach for Parameter Screening in Earthquake Simulation, High Performance Machine Learning Workshop, High Performance Machine Learn-
30   ing20Workshop, https://doi.org/10.1109/SBAC-PAD.2018.00062, 2018.

Moral, L., Gomez, J., Moreno, Y., and Pacheco, A.: Exact numerical solution for a time-dependent fibre-bundle model with continuous damage, Journal of Physics A: Mathematical and General, 34, 9983, 2001a.

Moral, L., Moreno, Y., Gómez, J., and Pacheco, A.: Time dependence of breakdown in a global fiber-bundle model with continuous damage, Physical Review E, 63, 066 106, 2001b.

35 Moreno, Y., Gómez, J., and Pacheco, A.: Self-organized criticality in a fibre-bundle-type model, Physica A: Statistical Mechanics and its Applications, 274, 400–409, 1999.

Moreno, Y., Correig, A., Gómez, J., and Pacheco, A.: A model for complex aftershock sequences, Journal of Geophysical Research: Solid Earth, 106, 6609–6619, 2001.

Nanjo, K. and Turcotte, D.: Damage and rheology in a fibre-bundle model, Geophysical journal international, 162, 859–866, 2005.

Nanjo, K., Nagahama, H., and Satomura, M.: Rates of aftershock decay and the fractal structure of active fault systems, Tectonophysics, 287, 173–186, 1998.

Norris, R. M. and Webb, R. W.: Geology of California, 1990.

5 Ogata, Y.: Seismicity analysis through Point-process modeling, Geophys J Int, 155, 471–507, 1999.

Olami, Z., Feder, H. J. S., and Christensen, K.: Self-organized criticality in a continuous, nonconservative cellular automaton modeling earthquakes, Physical Review Letters, 68, 1244, 1992.

Omori, F.: On the after-shocks of earthquakes, vol. 7, The University, 1894.

Ozturk, S.: Statistical correlation between b-value and fractal dimension regarding Turkish epicentre distribution, Earth Sciences Research
10   Journal, 16, 2012.

Peirce, F. T.: Tensile tests for cotton yarns:"the weakest link" theorems on the strength of long and of composite specimens, J. Textile Inst, 17, T355–368, 1926.

Phoenix, S. L.: Stochastic strength and fatigue of fiber bundles, International Journal of Fracture, 14, 327–344, 1978.

Phoenix, S. L. and Beyerlein, I.: Statistical strength theory for fibrous composite materials, Comprehensive composite materials, 1, 559–639,
15   2000.

Phoenix, S. L. and Tierney, L.: A statistical model for the time dependent failure of unidirectional composite materials under local elastic load-sharing among fibers, Engineering Fracture Mechanics, 18, 193–215, 1983.

Pradhan, S. and Chakrabarti, B. K.: Failure properties of fiber bundle models, International Journal of Modern Physics B, 17, 5565–5581, 2003.

20 Pradhan, S., Hansen, A., and Chakrabarti, B. K.: Failure processes in elastic fiber bundles, Reviews of modern physics, 82, 499, 2010.

Roy, P. and Ram, A.: A correlation integral approach to the study of 26 January 2001 Bhuj earthquake, Gujarat, India, Journal of Geodynamics, 41, 385–399, 2006.

Sadovskiy, M., Golubeva, T., Pisarenko, V., and Shnirman, M.: Characteristic dimensions of rock and hierarchical properties of seismicity, Izvestiya, Academy of Sciences, USSR. Physics of the solid Earth, 20, 87–96, 1984.

25 Savage, J. and Svarc, J.: Postseismic relaxation following the 1994 Mw6. 7 Northridge earthquake, southern California, Journal of Geophysical Research: Solid Earth, 115, 2010.

Scholz, C.: Spontaneous formation of space-time structures and criticality, ed. Riste, T. and Sherrington, D., p. 41, 1991.

Scholz, C. H.: The mechanics of earthquakes and faulting, Cambridge university press, 2002.

Segall, P. and Pollard, D.: Mechanics of discontinuous faults, Journal of Geophysical Research: Solid Earth, 85, 4337–4350, 1980.

30 Shi, Y. and Bolt, B. A.: The standard error of the magnitude-frequency b value, Bulletin of the Seismological Society of America, 72, 1677–1687, 1982.

Sornette, D.: Elasticity and failure of a set of elements loaded in parallel, Journal of Physics A: Mathematical and General, 22, L243, 1989.

Stein, R. S.: The role of stress transfer in earthquake occurrence, Nature, 402, 605, 1999.

Stein, R. S., King, G. C., and Lin, J.: Stress triggering of the 1994 M= 6.7 Northridge, California, earthquake by its predecessors, Science,
35   265, 1432–1435, 1994.

Stirling M.W., G. T.: Magnitude Scaling Relationships, GNS Science Miscellaneous Series, 42, 1–35, 2012.

Thio, H. K. and Kanamori, H.: Source complexity of the 1994 Northridge earthquake and its relation to aftershock mechanisms, Bulletin of the Seismological Society of America, 86, S84–S92, 1996.

Turcotte, D. L.: Fractals and chaos in geology and geophysics, Cambridge university press, 1997.

Turcotte, D. L., Newman, W. I., and Shcherbakov, R.: Micro and macroscopic models of rock fracture, Geophysical Journal International, 152, 718–728, 2003.

U.S.G.S., S.: The Magnitude 6.7 Northridge, California, Earthquake of 17 January 1994, Science, 266, 389–397, 1994.

5   Utsu, T. and Ogata, Y., M. R.: The centenary of the Omori formula for a decay law of aftershock activity, J. Phys. Earth, 43, 1–33, 1995.

Vázquez-Prada, M., Gómez, J., Moreno, Y., and Pacheco, A.: Time to failure of hierarchical load-transfer models of fracture, Physical Review E, 60, 2581, 1999.

Wallace, R. E.: Active faults, paleoseismology, and earthquake hazards in the western United States, Earthquake prediction, pp. 209–216, 1981.

10   Wesnousky, S. G.: The Gutenberg-Richter or characteristic earthquake distribution, which is it?, Bulletin of the Seismological Society of America, 84, 1940–1959, 1994.

Wiemer, S. and Wyss, M.: Minimum magnitude of completeness in earthquake catalogs: Examples from Alaska, the western United States, and Japan, Bulletin of the Seismological Society of America, 90, 859–869, 2000.

Yewande, O. E., Moreno, Y., Kun, F., Hidalgo, R. C., and Herrmann, H. J.: Time evolution of damage under variable ranges of load transfer, 15   Physical Review E, 68, 026 116, 2003.

Zuniga, F. R. and Wyss, M.: Most-and least-likely locations of large to great earthquakes along the Pacific coast of Mexico estimated from local recurrence times based on b-values, Bulletin of the Seismological Society of America, 91, 1717–1728, 2001.
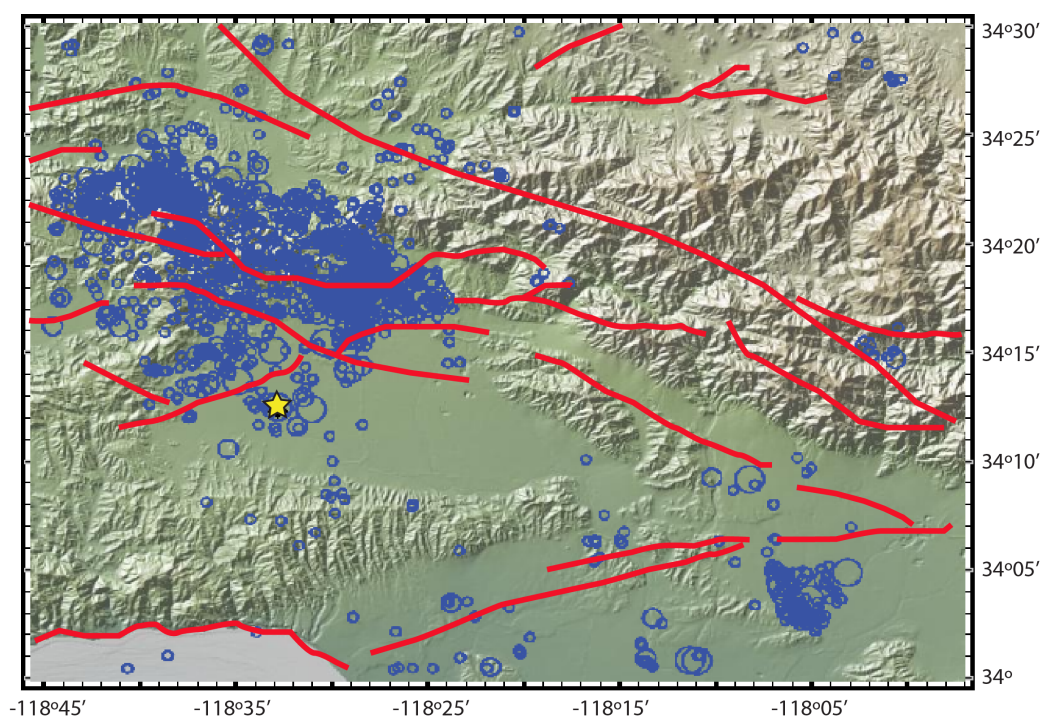
Figure 1. Map that includes the seismicity of magnitude larger than 2.0 during 1981-2006. Yellow star indicates the Northridge epicenter (M_w 6.7, 1994). Red lines depicts the faults of this region considering an approximated area of 0.6º x 0.6º (Turcotte, 1997)
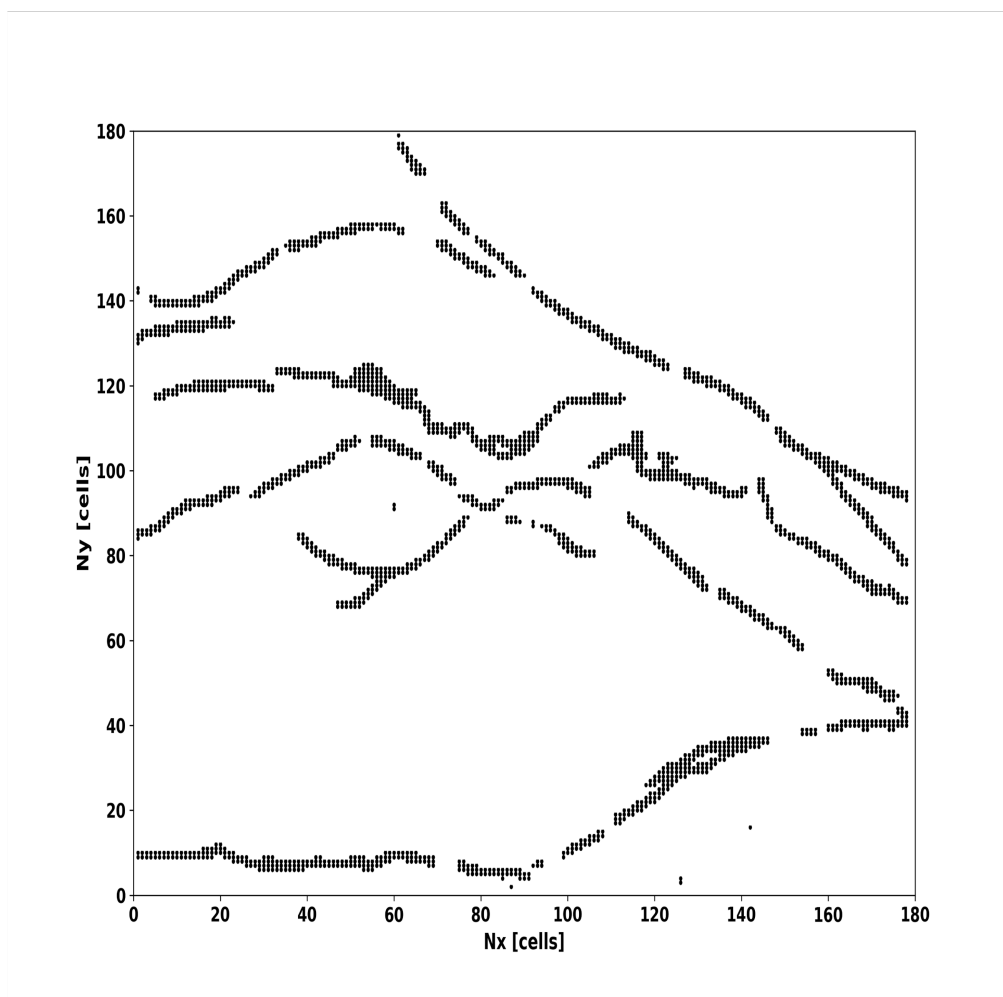
Figure 2. Discrete Northridge fault system (NOR).
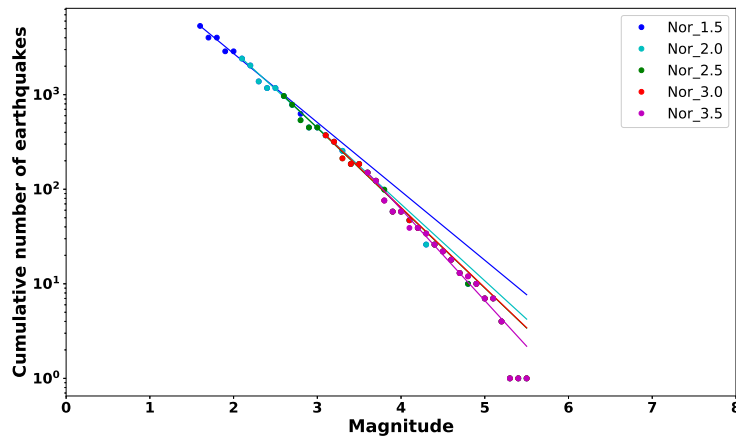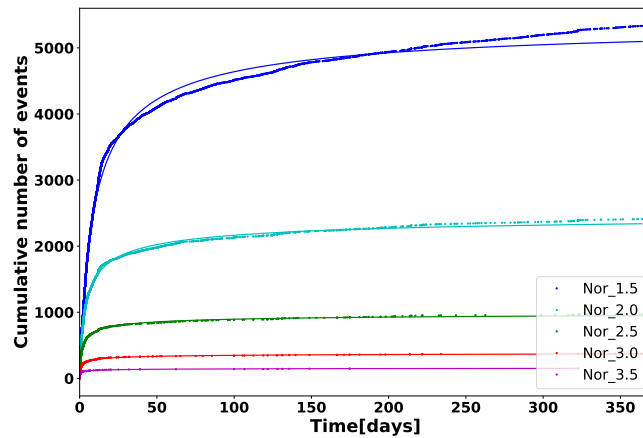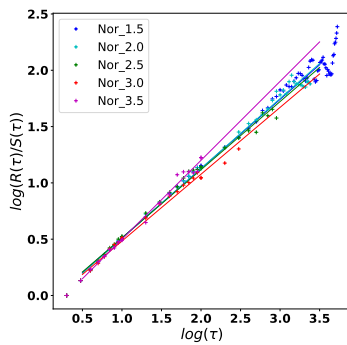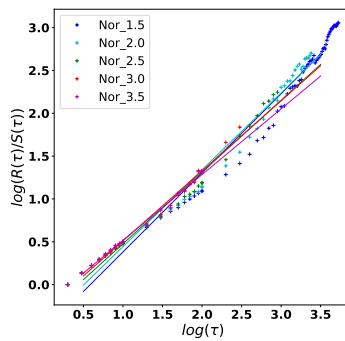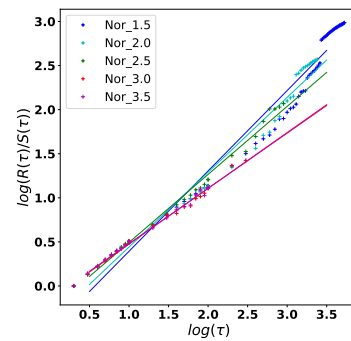
Figure 3. Fitting of (a) GR law, (b) MO law, and (c) Hurst exponent related to inter-event distance series, (d) Hurst exponent related to inter-event time series, (e) Hurst exponent related to magnitude series, to the Northridge aftershocks considering different minimum magnitude $M_{\min}$
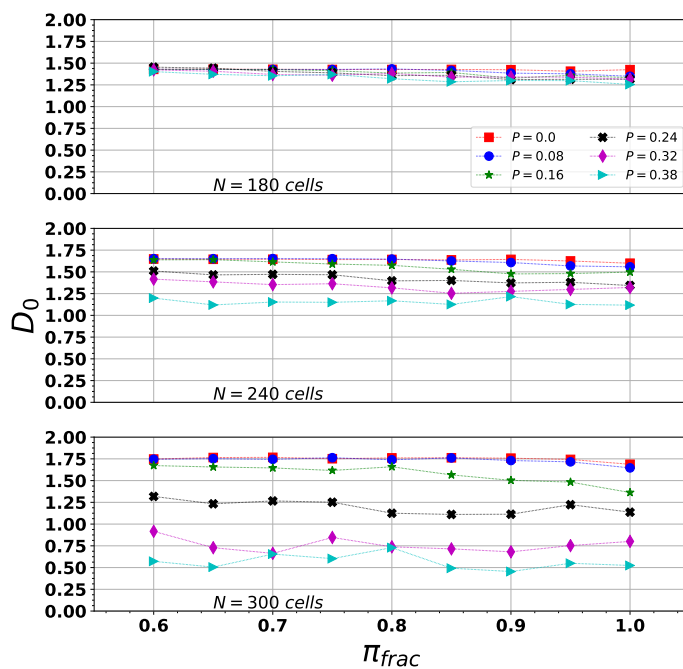
Figure 4. Fractal capacity dimension, D_0
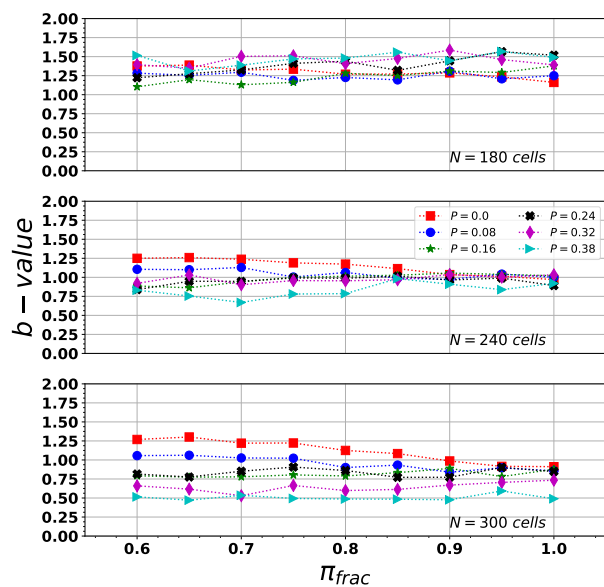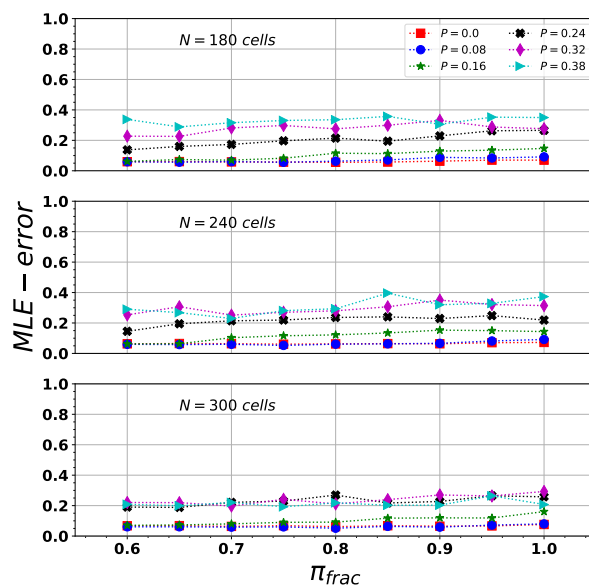
(a)   (b)

Figure 5. NOR b-value and MLE error
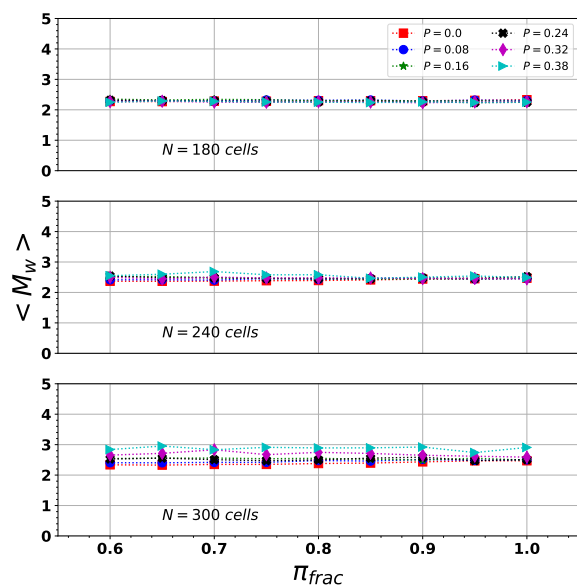
(a)
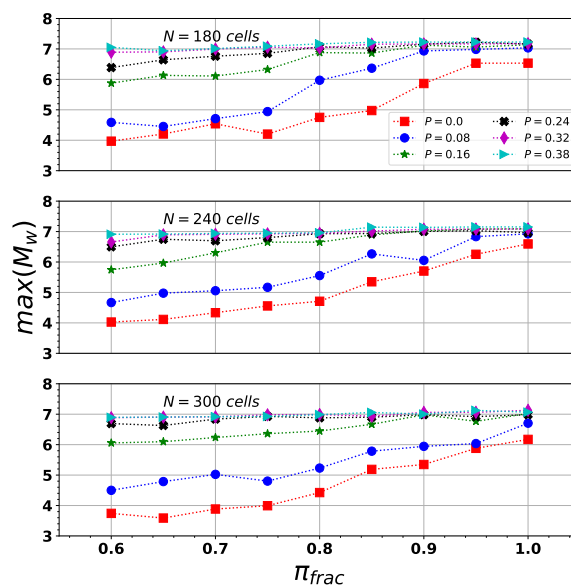
(b)

Figure 6. NOR mean and maximum magnitude
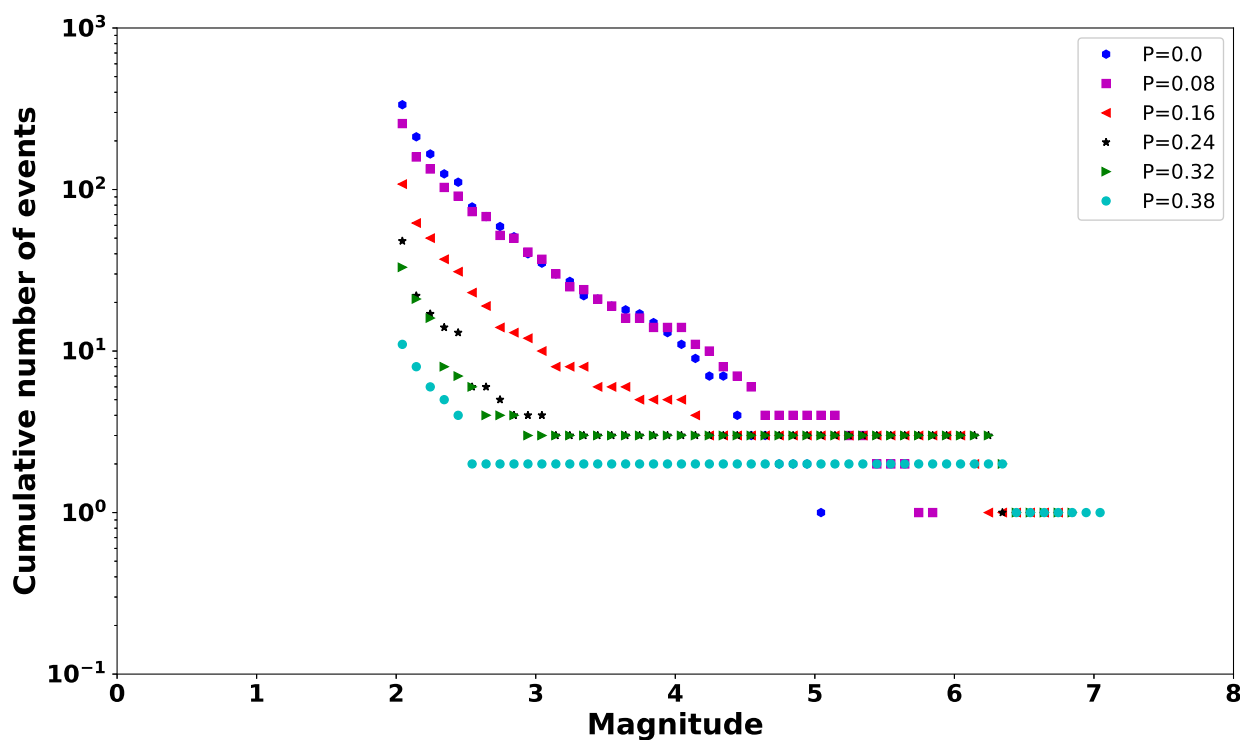
Figure 7. Example of the Frequency-Magnitude distribution of the synthetic series function of P

(a)   (b)
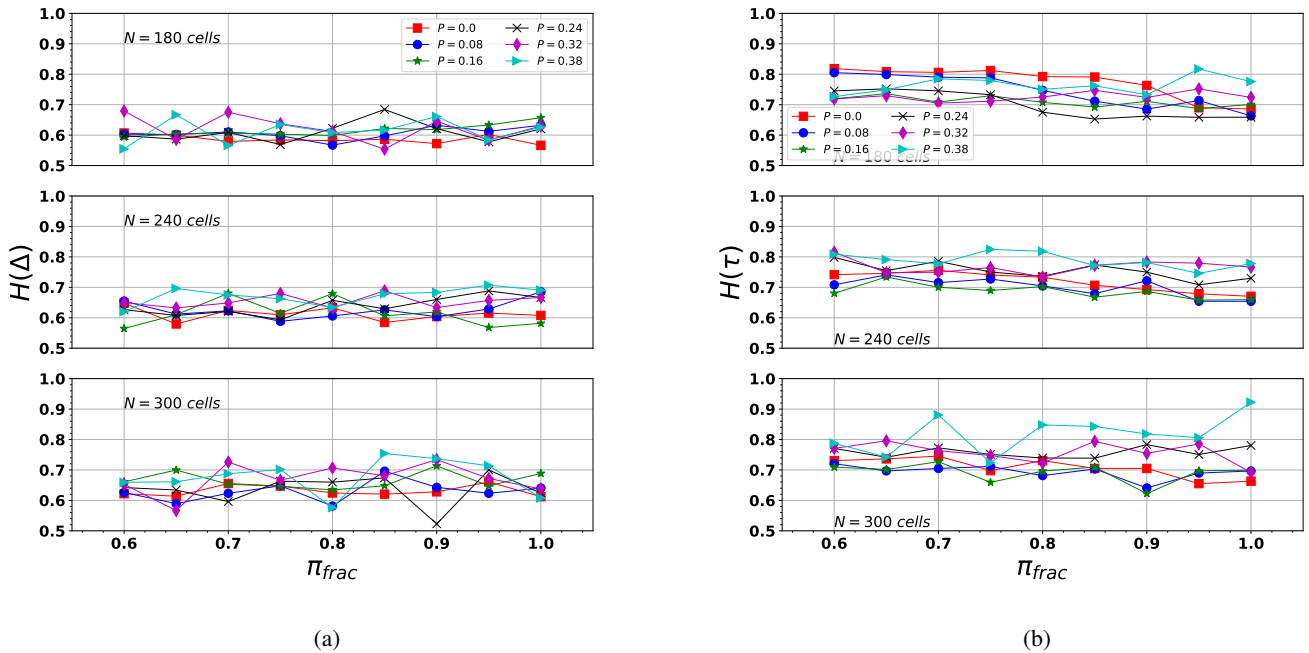
Figure 8. $H(\Delta)$ and $H(\tau)$ for NOR configuration
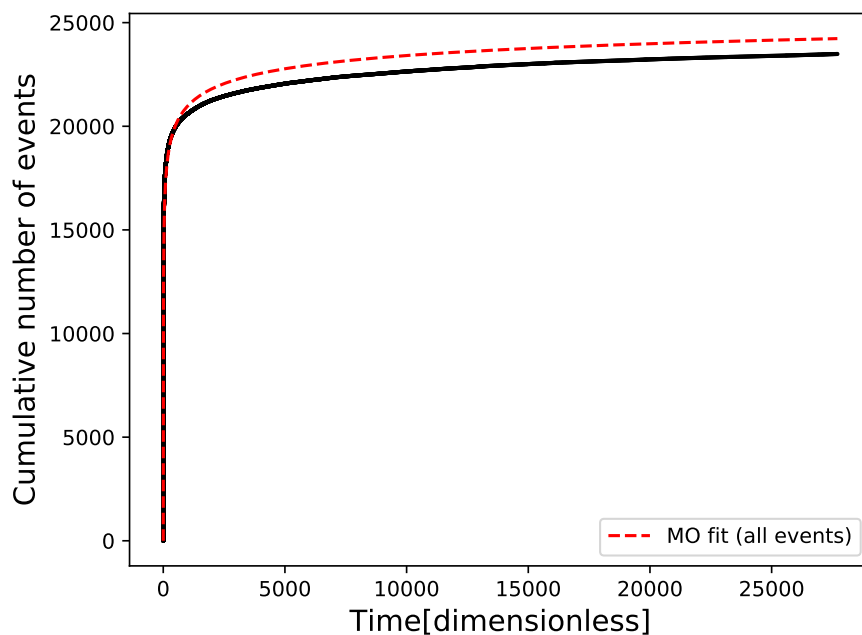
// (a)
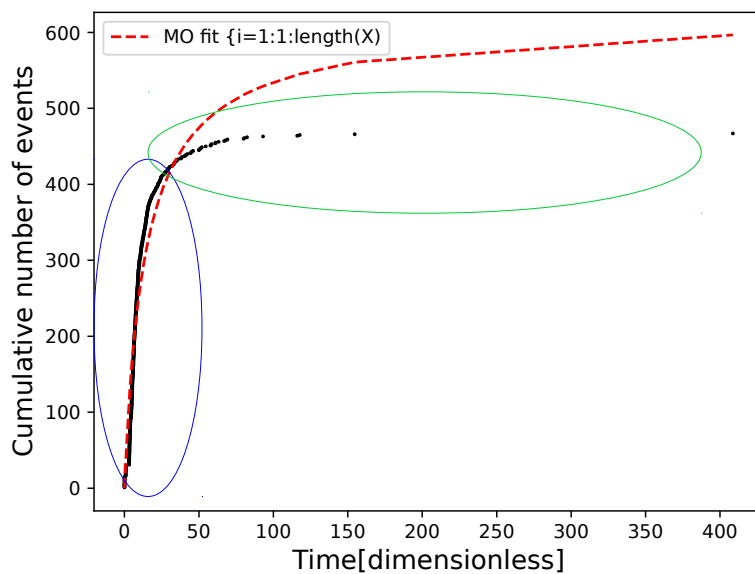
(b)

Figure 9. MO fit for a simulation with $P = 0.08$, $\pi_{\mathrm{frac}} = 0.90$, $N = 180$. a) simulated aftershock series for $M_{\min} = 2.0$. b) all events generated (minor and avalanches). Black dots are the simulated data and red curve the MOL fitting
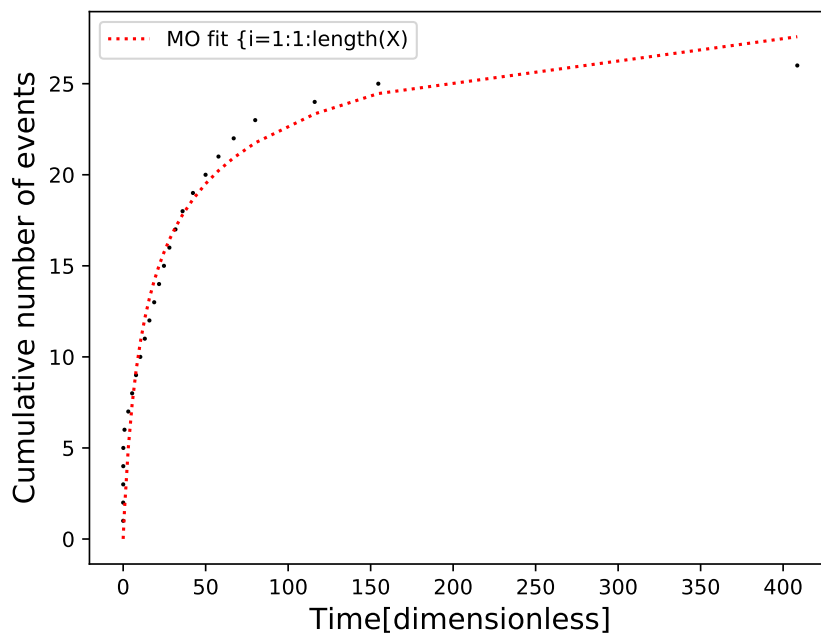
Figure 10. MOL fit of leading aftershock (LA) series
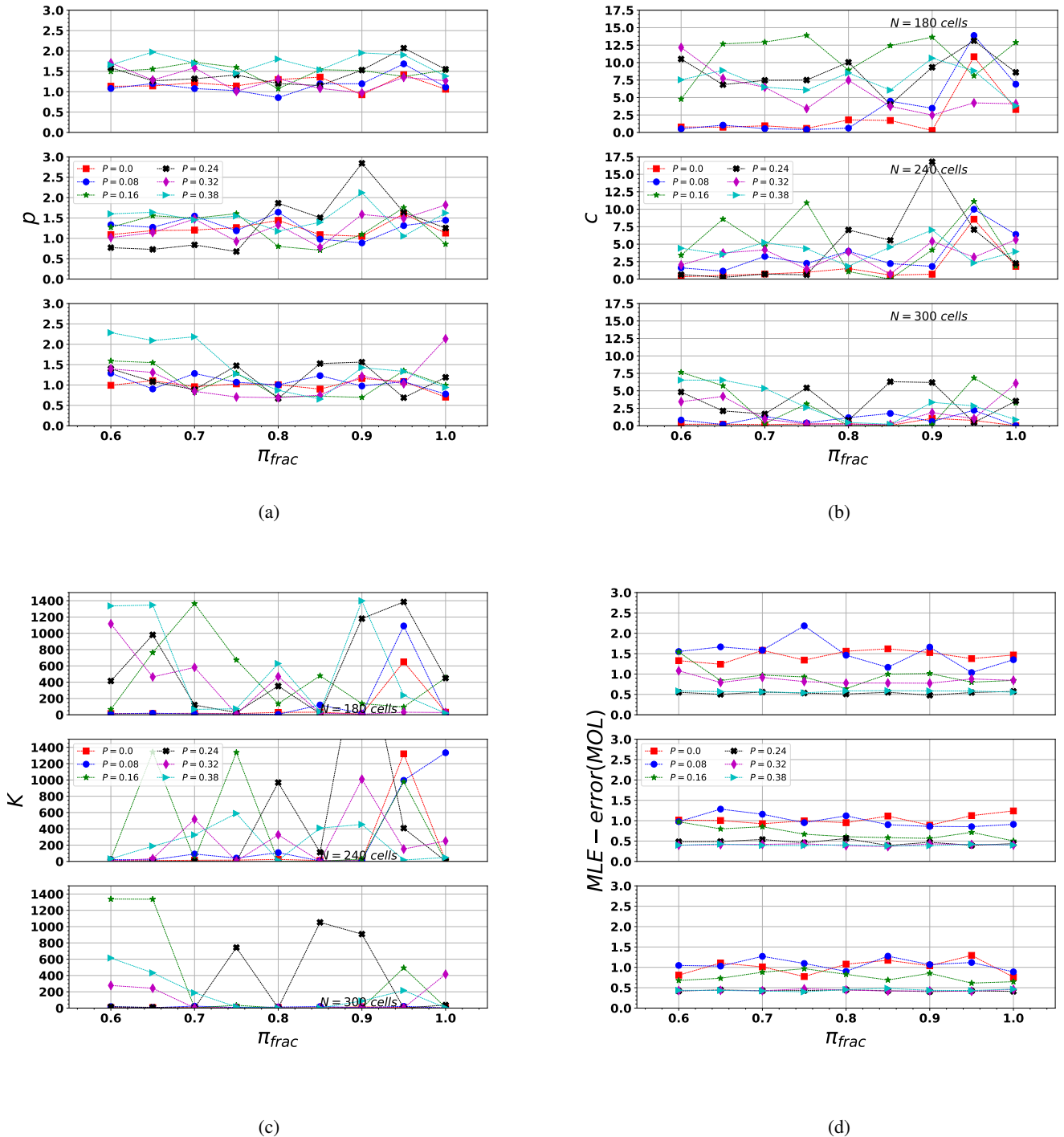
Figure 11. (a) p, (b) c, (c) K, and (d) rms values for LA synthetic series
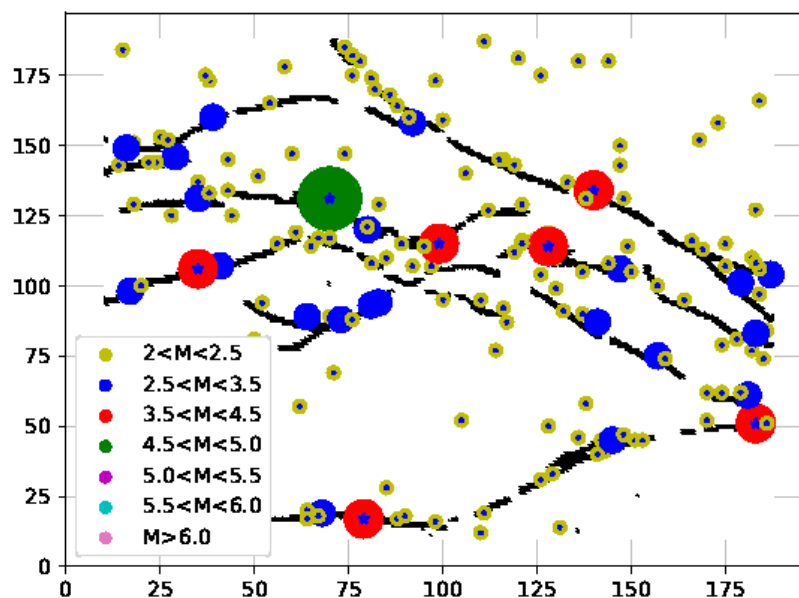
(a)
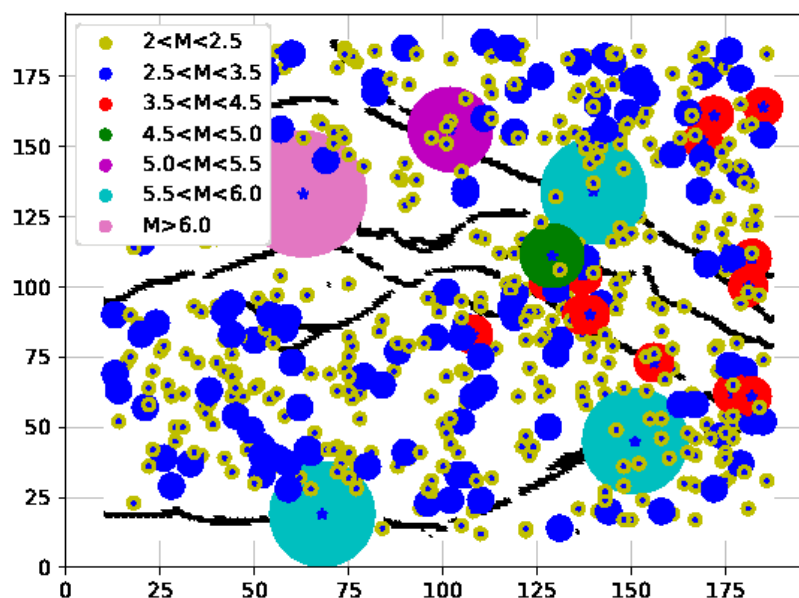
(b)

Figure 12. Two examples of the epicentral spatial distribution for $P = 0$, $\pi_{\mathrm{frac}} = 0.95$ and $N = 180$, (a) $\pi_{\mathrm{bkg}} = 0.25$, (b) $\pi_{\mathrm{bkg}} = 0.65$
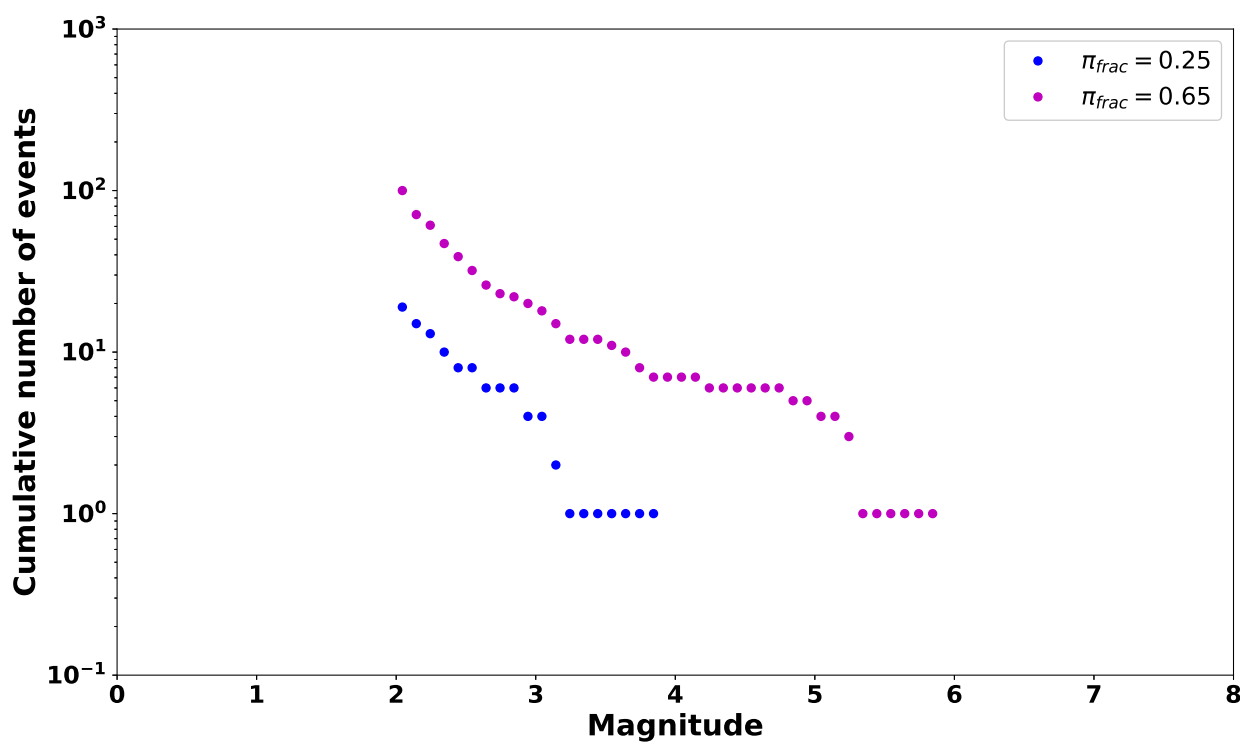
Figure 13. GR fit of simulated events for same values used in Fig. 12.
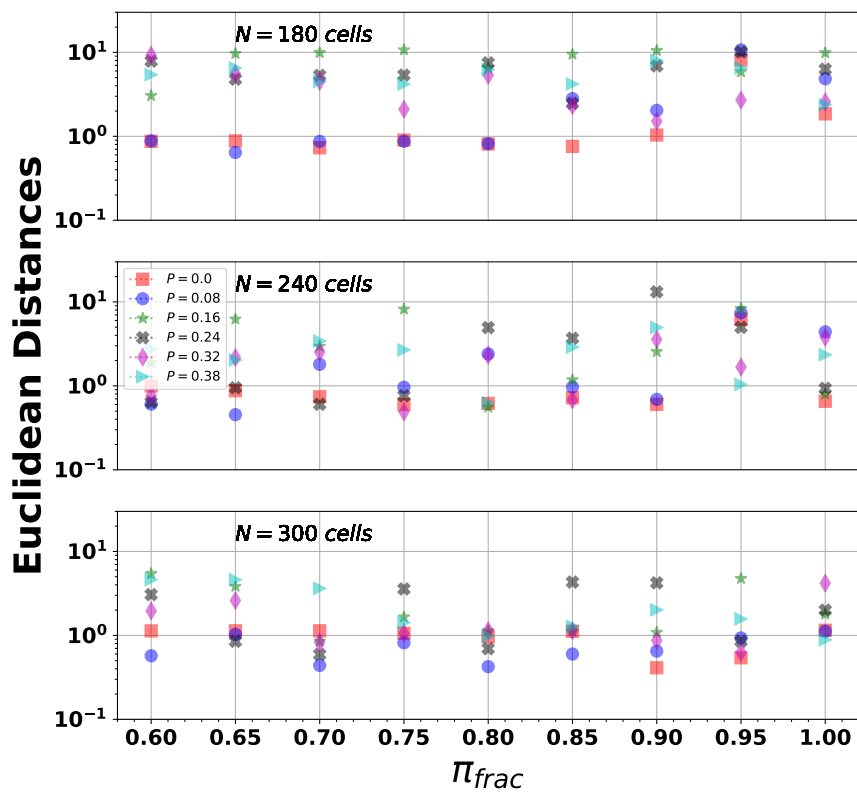
Figure 14. Euclidean distance $r_{\mathrm{E-Mmin}}$ computed for NOR series using $M_{\min} = 2.0$
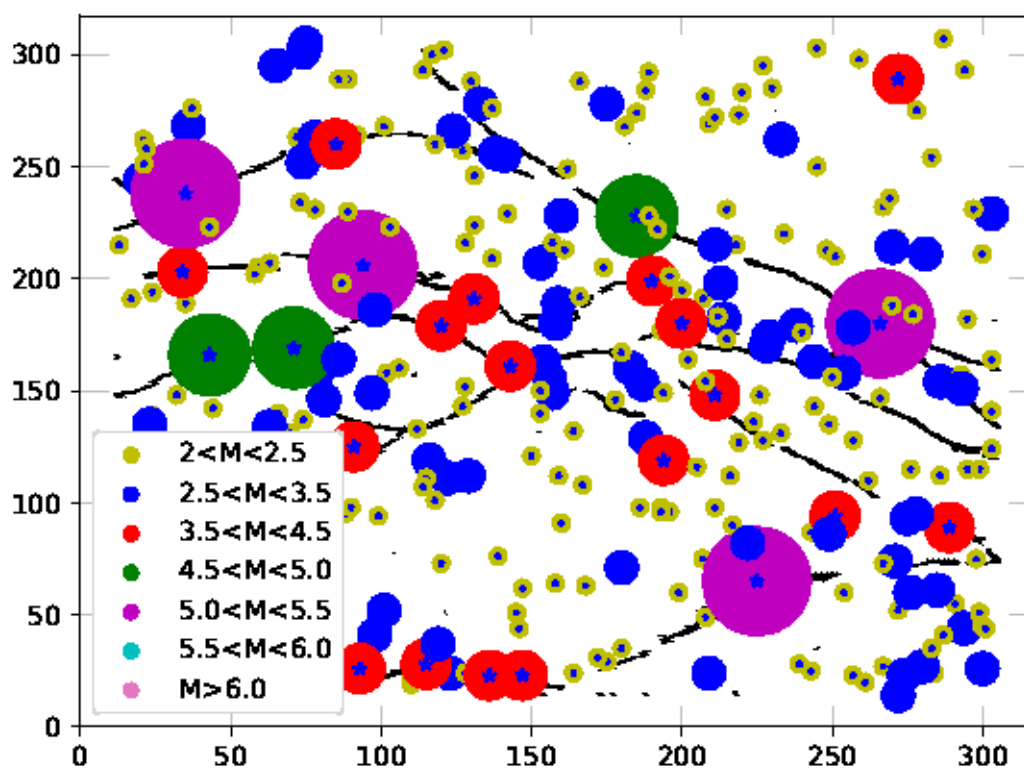
Figure 15. Example of the spatial distribution of simulated events for a particular FBM realization with $P = 0$, $\pi_{\text{frac}} = 0.95$ and $N = 300$. Circle areas depict the equivalent magnitude-area computed from Eq. 5. Star markers indicate the epicenter of each avalanche (simulated earthquake).
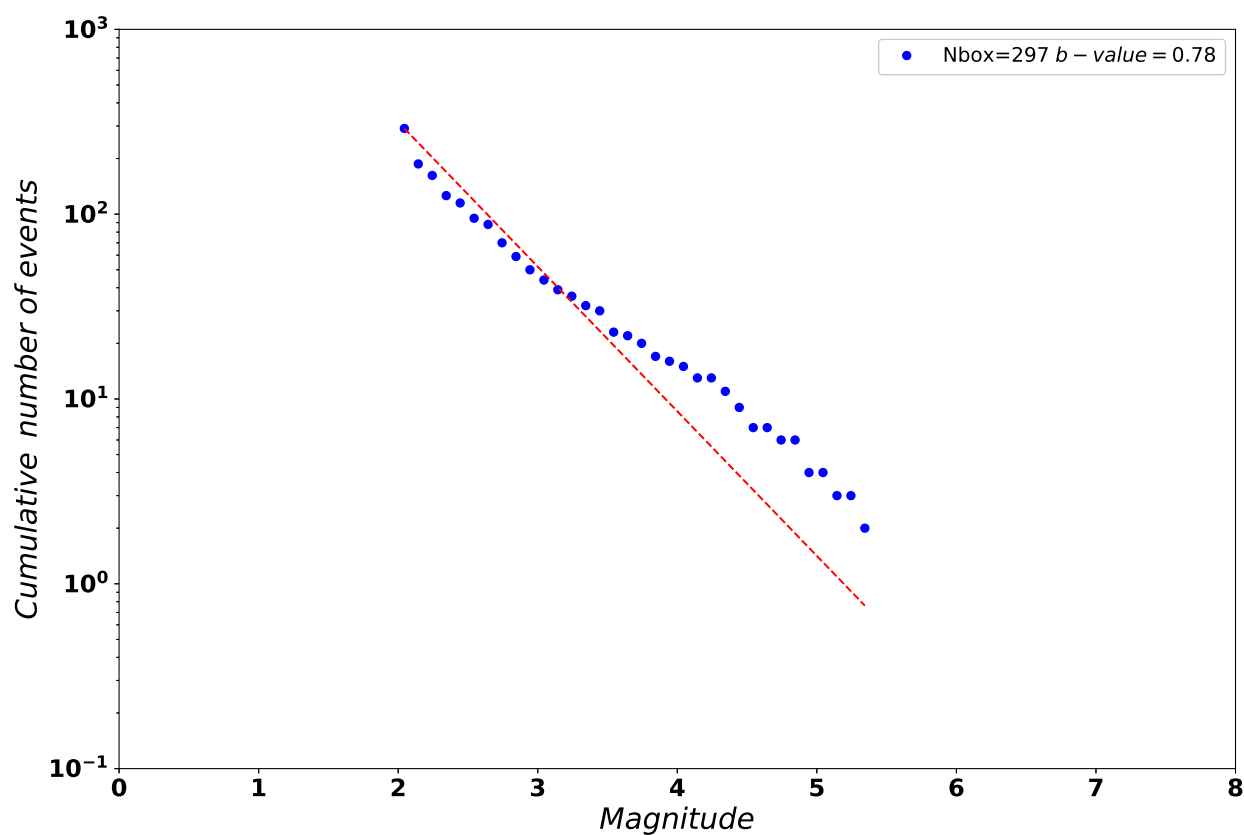
Figure 16. GR fit of simulated events ($P = 0$, $\pi_{\mathrm{frac}} = 0.95$, $\pi_{\mathrm{bkg}} = 0.65$ and $N = 300$).

Table 1. Empirical relations, interpretation and main parameters

Relation	Main parameters	Interpretation
Capacity Dimension (A1)	D_0	fractal measure of the epicentral spatial distribution
Rescaled Range (A6)	H	predictability of a inter-event time and inter-event distance series
Gutenberg-Richter (A7)	b-value	earthquake magnitude distribution
Omori-Utsu (A11)	c, K, p	temporal behavior of aftershocks

Table 2. Model parameters

Parameter	search range or value	definition
$\sigma(x,y)$	random initial value U[0,1]	load at each cell in (x,y) position
$\pi(x,y)$	[0.65, 0.70, 0.75, 0.80, 0.85, 0.90, 0.95, 1.0]	load transfer value
$F(x,y)$	Eq. 2	rupture probability
P	[0,0.08,0.16,0.24, 0.32, 0.38]	initial order probability
N_T	32400, 57600, 90000	total number of cells
ρ	Eq. 1	Weibull index

Table 3. Statistical parameters of the real catalog of Northridge aftershocks using different threshold magnitudes $M_{\min}$.

Parameter	$M_{\min} > 1.5$	> 2.0	> 2.5	> 3.0	> 3.5
N	5334	2412	970	373	151
D_0	1.58	1.48	1.49	1.40	1.27
$< M_w >$	2.15	2.59	3.07	3.57	4.55
b-value	0.73	0.81	0.84	0.84	0.88
p-Omori	1.35	1.32	1.31	1.24	1.18
c-Omori	3.22	1.19	0.40	0.13	0.03
K-Omori	3485.76	976.15	256.03	63.76	17.64
H_Δ	0.61	0.62	0.61	0.60	0.69
H_τ	0.92	0.90	0.83	0.81	0.76
$H_{Mag.}$	0.75	0.75	0.76	0.71	0.71

Table 4. minimum euclidean distance $r_{\mathrm{E}-\mathrm{M}_{\min}}$ (Eq. 7) using four different $M_{\min}$ NOR series (Table 3)

$M_{\min}$	$r_{E-M_{\min}}$	N	P	π_{frac}
1.5	0.78	240	0.16	0.6
2.0	0.63	300	0	0.95
2.5	0.88	300	0.08	0.9
3.0	1.53	300	0.16	0.7